Article

Aerosol depolarization ratio measurement capabilities for an elastic LIDAR: implementation and first measurements

Alejandro Rodríguez-Gómez[1*]; Michaël Sicard[1,2]; María-José Granados-Muñoz[1]; Enis Ben Chahed[1,3]; Constantino Muñoz-Porcar[1]; Rubén Barragán[1,2]; Adolfo Comerón[1]; Francesc Rocadenbosch[1,2]; Eric Vidal[4]

[1] *CommSensLab, Unidad de Excelencia María de Maeztu, BarcelonaTech University (UPC), Spain*
[2] *Ciències i Tecnologies de l'Espai - Centre de Recerca de l'Aeronàutica i de l'Espai / Institut d'Estudis Espacials de Catalunya (CTE-CRAE / IEEC), BarcelonaTech University (UPC), Spain*
[3] *Politecnico di Torino, Italy.*
[4] *UTC Fire & Security España SL, Spain*
* Correspondence: alejandro@tsc.upc.edu; Tel.: +34-93-4137237

Abstract: A new approach to the measurement with elastic lidar of depolarization produced by atmospheric aerosols is presented. The system uses two different telescopes: one for depolarization measurements and another for total-power measurements. The system architecture and principle of operation are described. The first experimental results are also presented, corresponding to a collection of atmospheric conditions over the city of Barcelona.

Keywords: Lidar system, depolarization channel, calibration, stability, depolarizing particles

1. Introduction

Multi-wavelength lidars provide a number of measurements that can be used to characterize the nature and origin of the aerosols present in the atmosphere. The most relevant [1] are: the lidar ratio, defined as that between the retrieved extinction and backscattering at a given wavelength; the ratio of lidar ratios at two different wavelengths and the color ratio (also known as the Ängstrom coefficient [2]), also computed by comparing the retrieved backscattering and extinction at different wavelengths.

Additionally, since the 1970s the use of the lidar depolarization technique has proven to be a valuable tool for atmospheric sciences, e.g. [3] or [4]. Regarding aerosol characterization, the depolarization information has been widely used for aerosol typing when combined with additional optical properties (e.g. [5–10]). In this sense, it can also be very useful in the retrieval of the planetary boundary layer (PBL) height since it allows to discriminate between the aerosol within this layer and different aerosol types coupled to the PBL height based on aerosol data [11]. Fig. 1 shows, in a very visual manner, how the depolarization data combined with the color ratio allow for discriminating among different kinds of aerosols and clouds. So depolarization information can be added to the set of parameters to be considered in aerosol classification [12,13].

Besides aerosol typing, the depolarization technique also provides relevant information for the retrieval of aerosol microphysical properties. Due to the particle shape information associated to lidar depolarization, retrievals of non-spherical particles by inversion methods can be highly improved (see e.g. [14–17]).

Preprints (www.preprints.org) | NOT PEER-REVIEWED | Posted: 13 October 2017 doi:10.20944/preprints201710.0095.v1

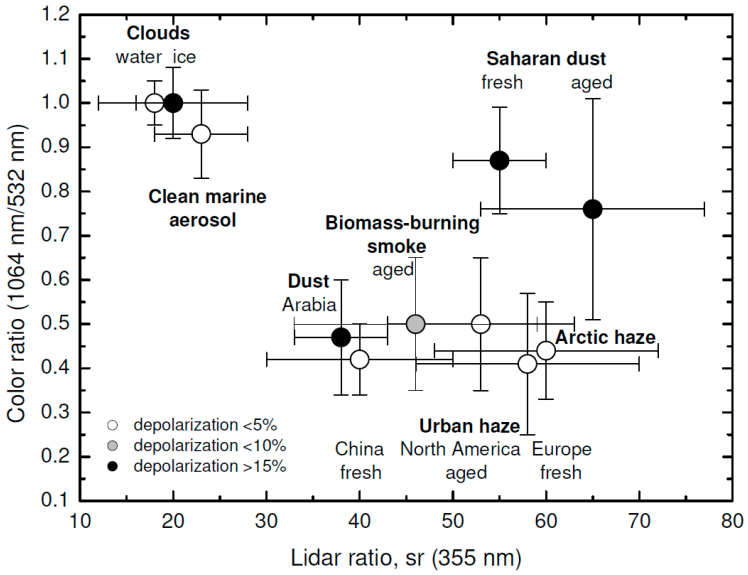

Fig. 1. Color ratio vs lidar ratio and particle depolarization ratio for different aerosol and cloud types. Figure from [18] with information from [1]. Reproduced with permission from the authors.

Because of the importance of depolarization measurements for aerosol science, a new depolarization measurement channel [19] has been developed and implemented for the BarcelonaTech (UPC) 6-channel elastic/Raman lidar [20]. The main difference with other present lidar systems with depolarization measurement capability (see, for instance, [21] or [22]) is the use of an additional telescope (in fact, a telephoto lens) to measure the cross-polarized return signal, without altering the rest of the original system.

Section 2 describes the system architecture; section 3 contains the basic formulation for retrieving the information about depolarization profiles; section 4 details the calibration process and section 5 presents some measurements corresponding to a collection of atmospheric conditions over the city of Barcelona.

2. System architecture

A complete description of the UPC main lidar instrument can be found at [20]. The transmitter is based on a Quantel® Brilliant® laser, equipped with second and third harmonic generators. The laser produces 3.6-ns pulses at with energies 130 mJ at 1064 nm and 532 nm and 40 mJ at 355 nm.

The 6-channel main receiver unit is sketched in Fig. 2. A 356-mm diameter telescope (CELESTRON® C14-A XLT) collects backscattered light and couples it (with the help of a field lens) to a 3-mm diameter fiber bundle (manufactured by CeramOptec®, custom-made). This bundle delivers the light to a poly-chromator, which splits the beam to the different channels. They include: three elastic backscattering channels (1064, 532 and 355 nm) and three Raman channels (607 and 387 nm for nitrogen and 407 nm for water vapor).

The axes of the laser beams and the telescope are parallel, with an approximate distance of 30 cm between them. This fact causes the partial overlap between the part of the atmosphere illuminated by the laser beams and that "seen" by the receivers, which affects to the amount of light collected from short distances [23].

Preprints (www.preprints.org) | NOT PEER-REVIEWED | Posted: 13 October 2017 doi:10.20944/preprints201710.0095.v1

We have tested the polarization performance of the fiber bundle [24], finding that, for a linearly polarized input, the circularity of the polarization ellipse of the light at the output is better than 93% (in power terms). This fact permits to consider that the 6 channels (including the 532-nm one) are basically sensitive to the total collected power, without any polarization discrimination, even though the poly-chromator includes several beam-splitters that could cause diattenuation. The overall calculated transmission of the fiber bundle and the poly-chromator at the 532-nm output is 6.18% [20]. Further measurements (see section **Error! Reference source not found.**) suggest that the 532-nm channel transmission could be lower.

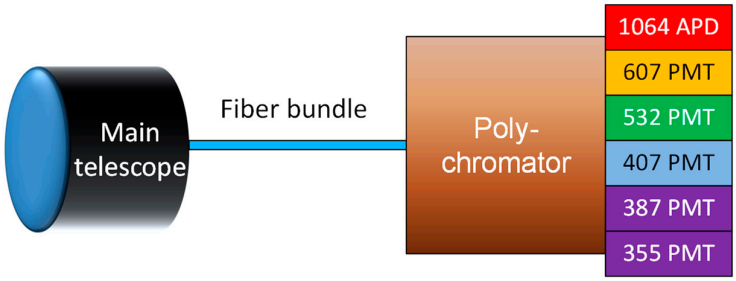

Fig. 2. Main receiver in UPC lidar [20].

The signal collected in the different channels is detected by means of an APD photo-receiver (for the 1064 nm channel) and five photo-multiplier tube modules (for the remaining channels) and digitized by a parallel Licel® Transient Recorder [25] with analog and photon-counting capabilities.

The aerosol depolarization ratio measurement requires the comparison of the signals recovered by two channels in the system: one proportional to the total power and another proportional to either the co-polar or cross-polar component of the signal collected [26]. These two channels operate at 532 nm.

The depolarization auxiliary channel [19,24,27] is shown in Fig. 3.

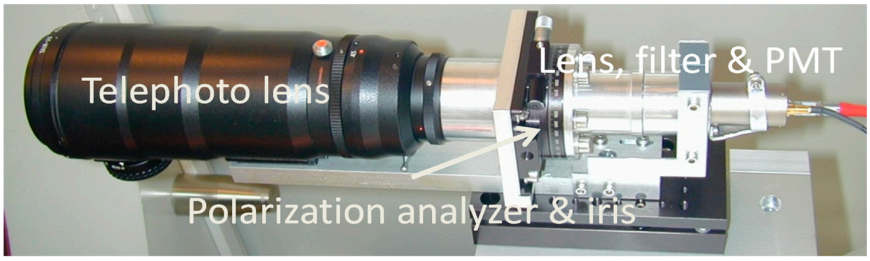

Fig. 3. Auxiliary channel for depolarization measurements, where the most relevant elements are labelled

The depolarization channel uses a separate telescope (a 70-mm aperture, 300-mm focal distance TAIR-3S telephoto lens). The rest of the optical arrangement, sketched in Fig. 4, includes a 1-mm field-of-view stop iris (D) in the focal plane, a polarization analyzer (P), and eye-piece lens (L4) and a Barr® interference filter (IF) centered at 532 nm, with 0.5-nm spectral width. The polarization analyzer is made by a linear polarizer mounted on a goniometric mount that can be seen in Fig. 3.

Preprints (www.preprints.org) | NOT PEER-REVIEWED | Posted: 13 October 2017 doi:10.20944/preprints201710.0095.v1

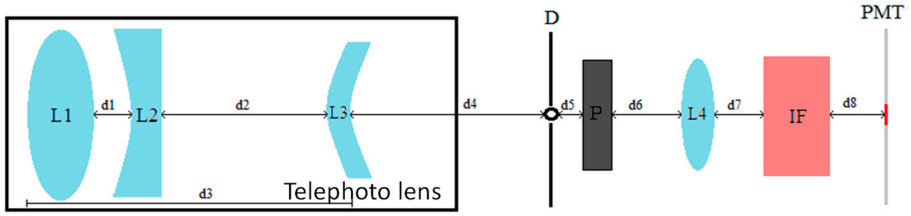

Fig. 4. Depolarization channel optical configuration

The different distances are indicated in Table 1. Some of the parameters provided in Table 1 have been experimentally determined and adjusted for an optimal performance of the depolarization channel. Every component (except for the telephoto lens) has a diameter of 2.54 mm.

Table 1. Parameters of the different optical elements of the depolarization channel.

Parameter	Value
d4	138.9 mm (estimated)
d5	1 mm
d6	39.4 mm
d7	5 mm
d8	23 mm
Telephoto lens focal distance	300 mm
Eye-piece lens focal distance	38 mm
Interference filter	
Center wavelength	531.9 nm
Spectral width	0.5 nm
Thickness	11 mm

The collected light is detected by the active surface of a Licel® R9880U PMT module (PMT in Fig. 4) [28], which feeds the detected current to a dedicated Licel® transient recorder.

The iris is located at the focal plane of the telephoto lens and limits the field of view to a theoretical value of 3.33 mrad (reduced partially due to building compromises, as it will be pointed out later), which is essential to limit the amount of background diffuse light that reaches the PMT active surface, as it is the reduced value of the filter spectral width; the eye-piece produces an image of the telephoto lens input aperture onto the PMT detection surface, optimizing the detection process.

A ray-optics simulation of the receiver has been performed, using the software ZEMAX®. Fig. 5 plots the axial ray distribution over the plane of the active surface of the photo-multiplier tube. The plot shows the impinging points of the rays parallel to the optical axis. The PMT active surface has an 8-mm diameter. According to the optical analysis, the r.m.s. diameter of the ray distribution is 6.2 mm, while all the traced rays lay within a 8.6-mm diameter, which leads to an expected 16% overspill.

 doi:10.20944/preprints201710.0095.v1

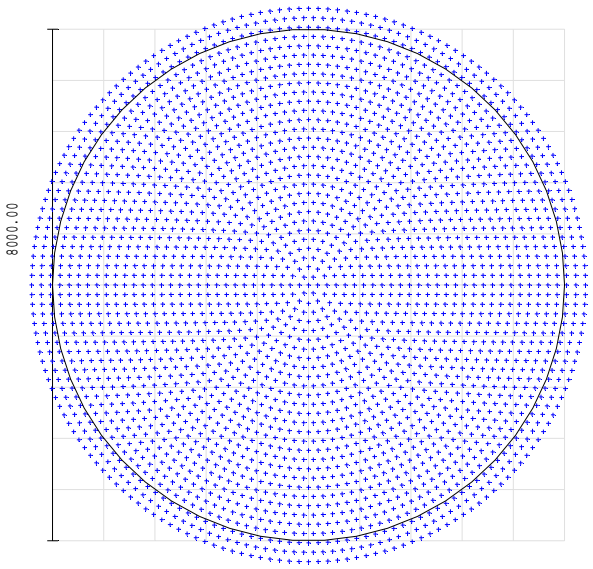

Fig. 5. Spot diagram of the distribution of the collected rays, parallel to the optical axis, over the 8-mm diameter active surface of the photo-multiplier detector tube calculated with ZEMAX® software.

Fig. 6 shows the ray distribution of those entering the telephoto lens with the maximum effective field of view which, according to the simulation has been reduced to 0.09 degrees (equal to a maximum effective field of view of the optical system of approximately 3.14 mrad). For these rays, the r.m.s. diameter is 6.15 mm and the maximum deviation from the center of the PMT active surface is 4.41 mm, which would lead to a maximum overspill of 22% approximately. The overall field of view (including only the rays that reach the PMT surface) is then reduced to approximately to 2.85 mrad.

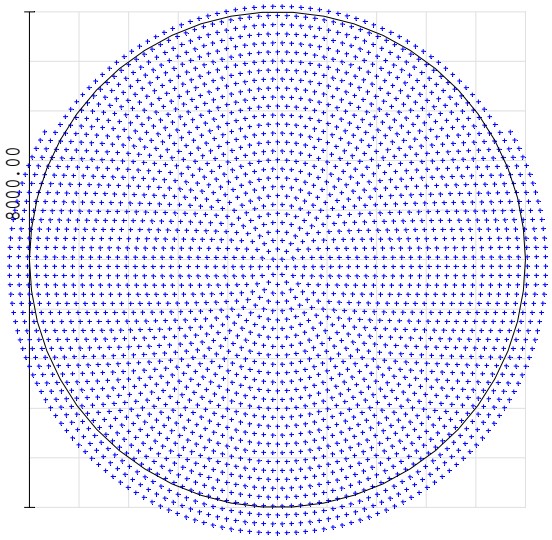

Fig. 6. Spot diagram of the distribution of the collected extreme rays, entering the optical system with an angle equal to half the effective field of view (0.09 deg), over the 8-mm diameter active surface of the photo-multiplier detector tube calculated with ZEMAX® software.

Preprints (www.preprints.org) | NOT PEER-REVIEWED | Posted: 13 October 2017 doi:10.20944/preprints201710.0095.v1

The telephoto lens axis is approximately 40 cm from the laser beams (refer to the laser description above), which affects to the partial overlap at short distances as indicated earlier in the text. Fig. 7 shows the complete system in our laboratory. The lidar is pointed in a vertical direction; whenever it is not been used, a motorized hose covers the equipment.

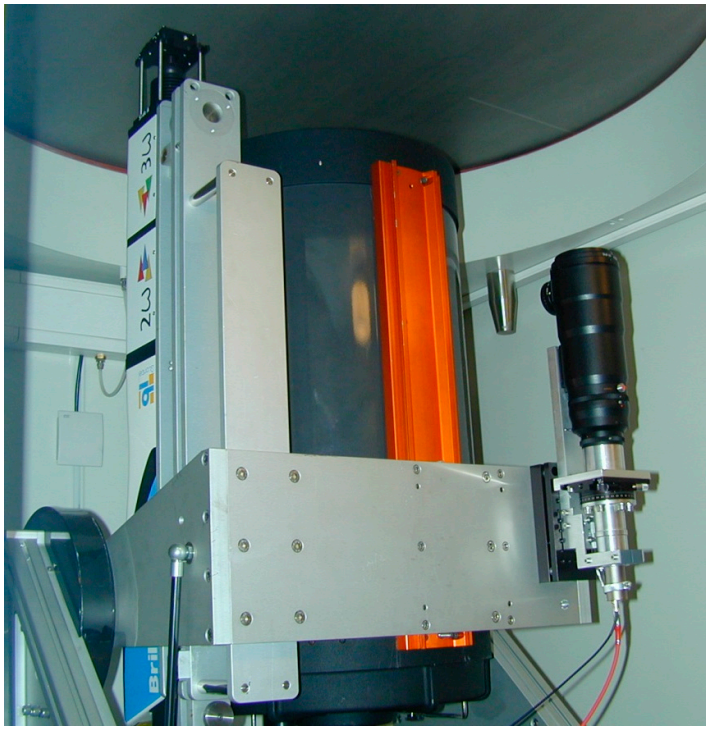

Fig. 7. Complete view of the UPC lidar system: the laser on the left (including 2nd and 3rd harmonic generators), the main telescope in the middle and the depolarization auxiliary channel on the right.

The nominal position of the polarization analyzer is 90-degrees from the transmitted beam polarization plane. In this way the channel is sensitive to the cross-polarized fraction of the light backscattered by the atmosphere.

3. Theory of operation

The lidar measures along a vertical axis, so in every expression the distance R to the lidar is equivalent to the height over the system.

The voltage signal obtained at the total-power PMT output can be written:

$$S_{Tot}(R) = V_{Tot}(R) \cdot P_{Tot}(R) \quad (1)$$

Where:

$V_{Tot}(R)$ is the total-power 532-nm channel responsivity, as a function of the distance to the lidar system R, including the effect of the partial overlap (see section **Error! Reference source not found.**).

$P_{Tot}(R)$ is the backscattered light power collected by the main telescope @532 nm.

The voltage signal obtained at the depolarization channel PMT output can be calculated:

$$S_{Dep}(90^{o}, R) = V_{Dep}(R) \cdot P_{\perp}(R) \quad (2)$$

Where:

Preprints (www.preprints.org) | NOT PEER-REVIEWED | Posted: 13 October 2017 doi:10.20944/preprints201710.0095.v1

$V_{Dep}(R)$ is the depolarization channel responsivity, as a function of the distance to the lidar system R, including the effect of the partial overlap.

$P_{\perp}(R)$ is the cross-polar fraction power of the depolarized backscattered light, function of R.

We will define the depolarization channel system function as:

$$V^{*}(R)=\frac{V_{Dep}(R)}{V_{Tot}(R)} \quad (3)$$

While it is extremely difficult to determine $V_{Dep}(R)$ and $V_{Tot}(R)$, it is possible to determine $V^{*}(R)$ by means of a calibration process that compares the output signals of the total-power channel and the cross-polar channel, when the polarization analyzer of the latter is set successively + and - 45 degrees from its nominal position [21]:

$$V^{*}(R)=2\sqrt{\frac{S_{Dep}(90^{o}-45^{o},R)}{S_{Tot}(R)}\times\frac{S_{Dep}(90^{o}+45^{o},R)}{S_{Tot}(R)}} \quad (4)$$

The factor 2 takes into account that, at the calibration positions, the auxiliary channel is detecting half of the total backscattered power.

The volume depolarization is usually defined [21]:

$$\delta^{V}(R)=\frac{P_{\perp}(R)}{P_{\parallel}(R)} \quad (5)$$

Accepting that $P_{Tot}(R)=P_{\parallel}(R)+P_{\perp}(R)$, and operating with the previous results, we can calculate the volume depolarization [24] as:

$$\delta^{V}(R)=\frac{\delta^{*}(90^{o},R)}{V^{*}(R)-\delta^{*}(90^{o},R)} \quad (6)$$

Where:

$$\delta^{*}(90^{o},R)=\frac{S_{Dep}(90^{o},R)}{S_{TOT}(R)} \quad (7)$$

Finally, the particle depolarization ratio can be computed by combining the volume ratio with the molecular and aerosol backscattering profiles [21]:

$$\delta^{p}(R)=\frac{\left[1+\delta^{m}\right]\cdot\delta^{V}(R)\cdot\rho(R)-\left[1+\delta^{V}(R)\right]\cdot\delta^{m}}{\left[1+\delta^{m}\right]\cdot\rho(R)-\left[1+\delta^{V}(R)\right]} \quad (8)$$

Where:

$$\rho(R)=\frac{\beta^{m}(R)+\beta^{p}(R)}{\beta^{m}(R)} \quad (9)$$

With $\beta^{m}(R)$ and $\beta^{p}(R)$, molecular and aerosol backscattering profiles retrieved by means of a Klett –Fernald ([29], [30]) or Raman ([31], [32]) inversion performed over the signal of the total-power channel.

Finally, the molecular volume depolarization ratio

$$\delta^{m}=\frac{\beta^{m}_{\perp}}{\beta^{m}_{//}} \quad (10)$$

was computed by Behrendt and Nakamura [33] and has an approximately constant value of 3.8×10-3 for a receiver with a spectral width of 0.5 nm.

Preprints (www.preprints.org) | NOT PEER-REVIEWED | Posted: 13 October 2017 doi:10.20944/preprints201710.0095.v1

The error analysis of the different magnitudes obtained in the data analysis is detailed in the appendix.

4. Calibration process

The determination of the depolarization channel system function is made by means of a calibration procedure that compares the outputs of the depolarization and the total power channels [21,35,36]; during the calibration the polarization analyzer of the depolarization channel is set first at +45 degrees, and second at -45 degrees from the nominal (cross-polar) position. Each one of the calibrations runs for 15 minutes, which amounts 18000 laser pulses.

The outputs of the two channels are divided and then a geometrical average is computed (as indicated in equation (4)) between the system profiles obtained at the two positions; after that a zero-phase low-pass spatial filter is applied to the average, to reduce noise effects; finally, the values obtained for heights over ~10km are discarded, also due to noise effects, considering the value obtained at 10 km for greater height values.

A number of calibrations have been performed since the implementation of the depolarization channel, and the historic is presented in Fig. 8. The color sequence shows the time evolution of the estimated system functions. As the colder colors point out, the early functions were affected by misalignments between the laser and the receiver. The most recent calibrations are stabilized to a medium-height value around 4.

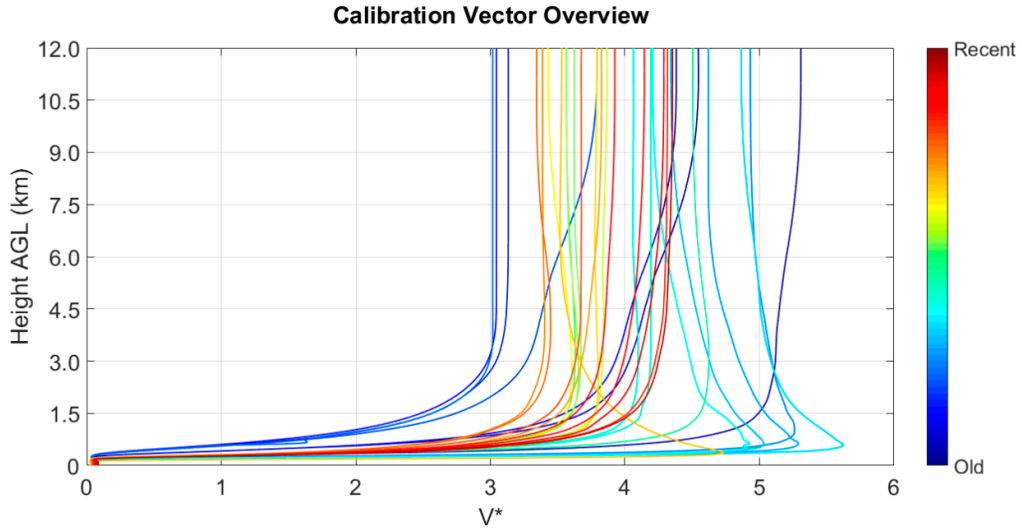

Fig. 8. Historic of the calibrations of the depolarization channel system function obtained from March 2016 to June 2017. The colder colors refer to early calibrations while the warmer ones to the recent ones.

Fig. 9 shows the temporal evolution of the far range value of V^* for the different calibrations presented in Fig. 8 with the values obtained between realignment procedures grouped. The first group of calibrations shows a deviation of more than 30%. After this period, an improvement in the anchorage of the receiving optics was implemented and the deviation was reduced to less than 10%, which was maintained after following realignment procedures. Anyway this diagram points out that different phenomena (thermal changes, mechanical relaxation, state of the atmosphere) affect V^* in a way that cannot be ignored.

Preprints (www.preprints.org) | NOT PEER-REVIEWED | Posted: 13 October 2017 doi:10.20944/preprints201710.0095.v1

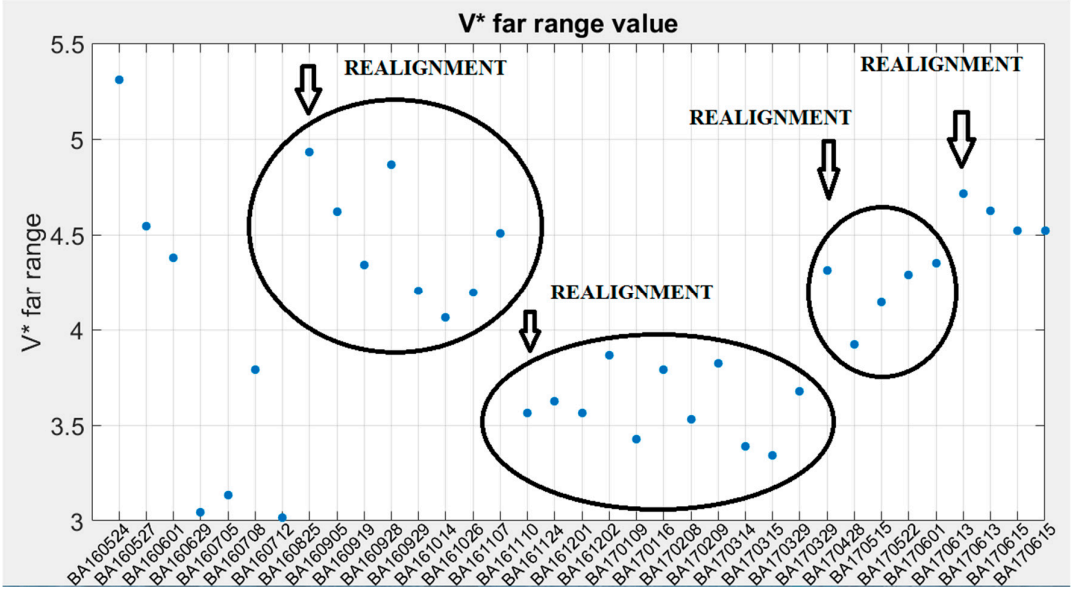

Fig. 9. Stability of the value of the depolarization channel system function for far range; the values comprised between realignment actions are marked by closed curves.

The system function includes the effect of the different overlap functions of the two channels; it also draws attention on the fact that, even though the ratio of the main telescope and the telephoto lens collecting surfaces is approximately 25, the depolarization channel optics has a higher transmission and a more responsive PMT receiver. This result also suggests that the transmission of the 532-nm total-power channel must be lower than that indicated in section **Error! Reference source not found.**. These uncertainties make the periodic calibrations unavoidable.

5. Depolarization ratio measurements

Some depolarization measurements are presented next for different aerosol loads. The volume depolarization ratio is retrieved from both total and perpendicular signals with Eq. (6) and a calibration depolarization channel system function, V^*. In all cases the depolarization channel system function is taken from the closest (in time) calibration performed prior to the measurement considered. The particle depolarization ratio is then retrieved with Eq. (8) from the volume depolarization ratio and the particle backscatter coefficient, β^p. All cases presented are daytime measurements, so that no Raman inversion is possible and thus β^p is retrieved with the Klett – Fernald ([29], [30]) method and a constant lidar ratio of 50 sr, except in the cirrus cloud case. In this case, as there is a molecular region below and above the cloud, the iterative backward-forward method [36] was applied to invert the cloud backscatter and extinction coefficients without the need to assume a lidar ratio. All profiles of the molecule backscatter coefficient, β^m, are calculated with the closest (in time) radiosoundings either at 12 or 00 UT. The error bars are calculated following the equations detailed in the appendix. For the sake of clarity, the points of the profiles of the particle depolarization ratio for which the error bar is larger than 50 % are not represented.

Fig. 10 shows the retrieval of volume and particle depolarization for different aerosol loads: pollen, mineral dust, fire smoke and a case of local urban aerosol, as well as a cirrus cloud case. In the case of pollen (Fig. 10a) the atmospheric boundary layer (ABL) extends up to ~1.5 km. In this layer δ^V is rather constant ~0.055 while δ^p varies slightly between 0.10 and 0.13. These values are in agreement with depolarization ratios measured during another pollen event in Barcelona by [37] who found mean values of δ^V (δ^p) of 0.06-0.10 (0.11-0.18) averaged over the period 9 – 17 UT.

 doi:10.20944/preprints201710.0095.v1

For the day considered here, 14th March, 2017, [38] counted a total pollen near-surface concentration in Barcelona of 1746 grains per cubic meter, being 90 % of them Platanus, which is in the lower range of values 1082-2830 found in [37]. The second case (Fig. 10b) gives typical values of depolarization for mineral dust. It is taken from an outstanding desert dust intrusion over Iberia with aerosol optical depths as large as 2 [39]. Above 1 km δ^V is in the range 0.17-0.24 and δ^p in the range 0.23-0.28. The small differences between δ^V and δ^p are due to the high values of the particle backscatter coefficient (~15 Mm-1sr-1) in the dust layer. According to [40] the values of δ^p found in our work are in the upper range of desert dust mixtures (0.14-0.28) and below the values of pure desert dust (0.30-0.35). The example shown in Fig. 10c illustrates the transport of Canadian fires over the Iberian Peninsula on 24th May, 2016, at 15 UT. The smoke layers were first detected on the evening of 22nd May (see Barcelona Micro Pulse Lidar quicklooks at https://mplnet.gsfc.nasa.gov/data?v=V3&s=Barcelona&t=20160522) and lasted until the evening of 24th May. In Fig. 9b one sees the fire smoke layer at ~2 km and a dust layer above 3 km. To illustrate a case of fire smoke, we looked into our short database but unfortunately we could not find a situation clearly identified as fire smoke and with no other aerosol type. In the fire smoke plume δ^p varies in the range 0.05-0.10. Here again our findings are in agreement with the literature, in particular with [40] which collects values of δ^p for pure biomass burning measured in several places around the globe in the range 0.02-0.08, being values of fresh smoke slightly lower than for aged smoke. Our values fall into the interval representative of aged smoke. We extend now the illustration of particle depolarization ratios retrieved with the UPC new depolarization channel to ice particles in cirrus clouds. Fig. 10d shows a case of cirrus clouds extending between 10 and 12.2 km with a rather clean troposphere below. The application of the iterative backward-forward method [36] gives a mean cirrus lidar ratio of 19 sr and a cirrus optical depth of 0.19. The cirrus cloud is quite heterogeneous in time and vertical range during the 60 min. of the measurements, which results in a large variability of the particle depolarization ratio which varies between 0.20 and 0.52, being the mean value 0.39±0.11. This high value of δ^p is in agreement with former studies such as [41] who found values in the range 0.30-0.45 for cirrus clouds at ~9.5-11.5 km height observed in north-central Oklahoma. Finally to give an idea of the particle depolarization ratio in background conditions in Barcelona, i.e. when the aerosol is from local urban origin and probably mixed with marine particles, a case without long-range transport is selected (Fig. 10e). The ABL is developed up to 1.25 km. δ^p is nearly constant and its mean value is 0.066±0.005. If we compare this value to the collection of depolarization ratios of [40] measured around the globe for anthropogenic pollution (0.06-0.10) and marine aerosols in different relative humidity conditions (0.01-0.10) we find a good agreement. However, at this point, from the depolarization ratio alone it does not seem possible to distinguish the fractions of anthropogenic pollution and of marine particles.

Preprints (www.preprints.org) | NOT PEER-REVIEWED | Posted: 13 October 2017 doi:10.20944/preprints201710.0095.v1

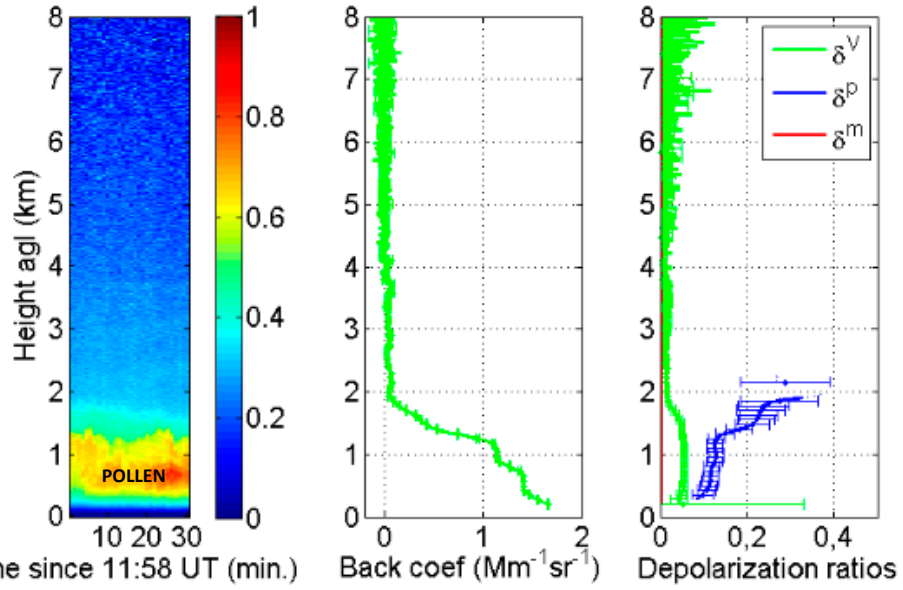

(a)

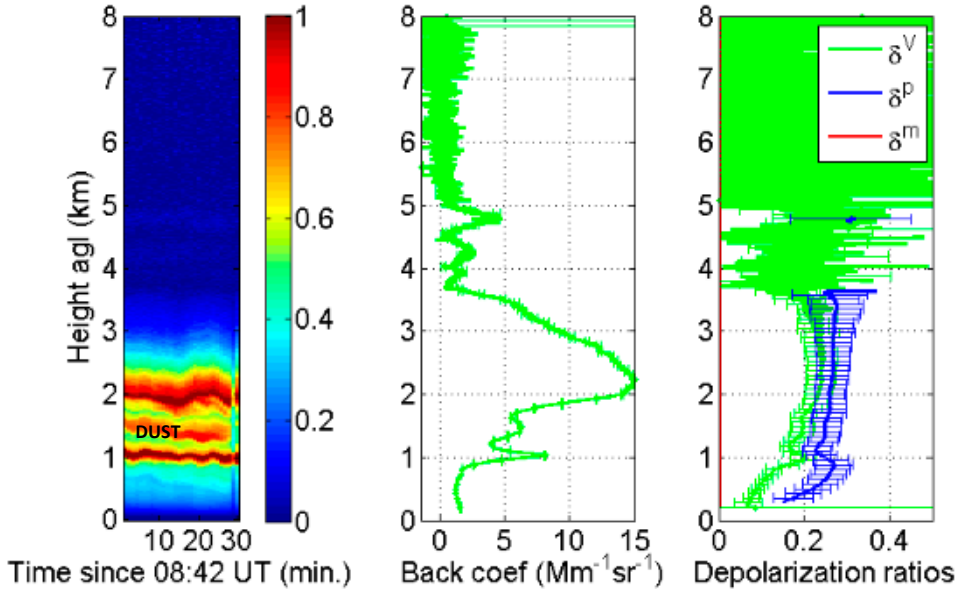

(b)

Preprints (www.preprints.org) | NOT PEER-REVIEWED | Posted: 13 October 2017 doi:10.20944/preprints201710.0095.v1

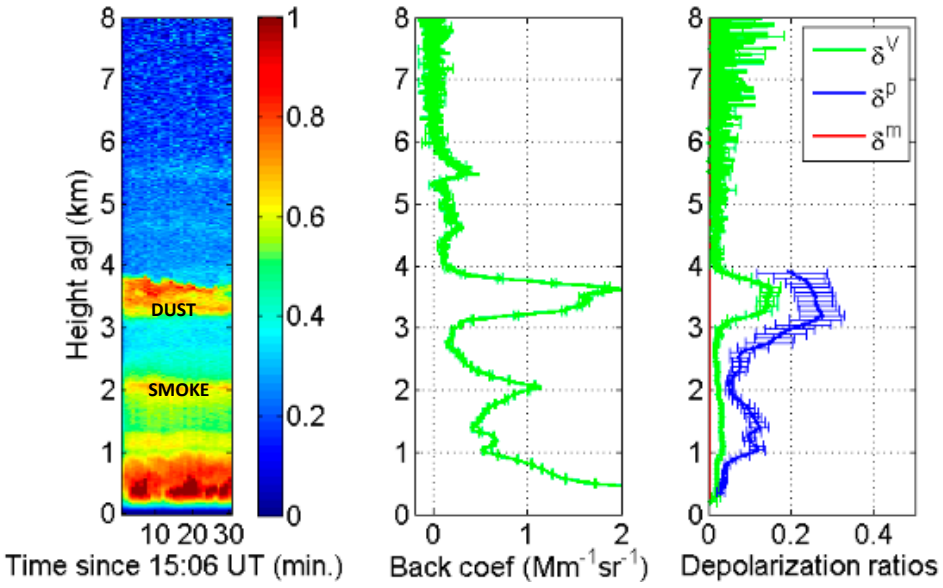

(c)

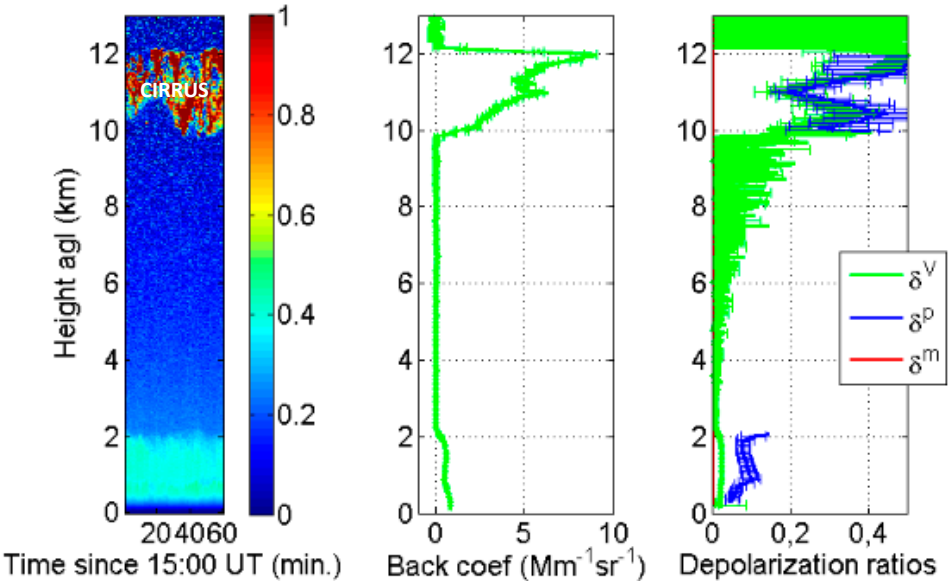

(d)

Preprints (www.preprints.org) | NOT PEER-REVIEWED | Posted: 13 October 2017 doi:10.20944/preprints201710.0095.v1

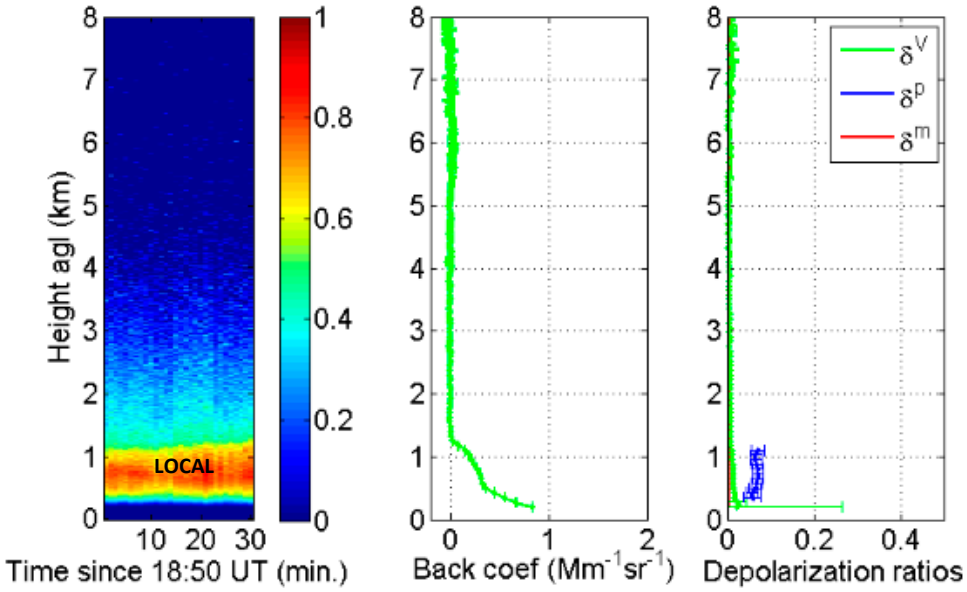

(e)

Fig. 10. Some examples of volume and particle depolarization ratio retrievals showing (left) time-height plots of range-square corrected signals in arbitrary units, (center) particle backscatter coefficient at 532 nm, (right) volume and particle depolarization ratios at 532 nm for (a) pollen, (b) dust, (c) dust and fire smoke, (d) cirrus cloud, (e) local urban. The points of the particle depolarization ratio profiles for which the associated error is larger than 50 % are not represented.

6. Conclusions

A new depolarization sensing subsystem has been implemented to a 6-channel elastic/Raman lidar. The architecture is based on a dedicated sub-telescope (a telephoto lens). The theory of operation has been presented, including the calibration procedure. Measurements performed during two Saharan dust intrusion events are used to test the new channel. Particle depolarization ratios varying between 10 and 40 % are found in the dust layers. Comparisons of the volume depolarization with an MPL system show a good agreement between both systems and demonstrate the reliability of the new depolarization channel of the UPC multi-wavelength lidar.

Acknowledgements

This work has been financed by the European Union (H2020, grant 654169, ACTRIS-2), the European Fund for Regional Development, the Spanish Government (grant TEC2015-63832-P) and the Catalan Government (grant 2014 SGR 583) and the Unidad de Excelencia Maria de Maeztu MDM-2016-0600, which is financed by the Agencia Estatal de Investigación, Spain. This work was supported by the "Juan de la Cierva-Formación" program (grant FJCI-2015-23904).

The authors also wish to acknowledge the priceless contribution of Joaquim Giner, Josep Pastor, Rubén Tardío and Albert Marton from the UPC technical staff.

Appendix: error estimation

The error analysis presented in this section is based in the well-known technique of the error propagation. If we have a function y that depends on n uncorrelated variables x_i:

Preprints (www.preprints.org) | NOT PEER-REVIEWED | Posted: 13 October 2017 doi:10.20944/preprints201710.0095.v1

$$y = f\left(x_1, x_2, ..., x_n\right) \tag{11}$$

Which are known with a standard deviation Δx_i

The most reliable value of y can be computed as:

$$\bar{y} = f\left(\bar{x}_1, \bar{x}_2, ..., \bar{x}_n\right) \tag{12}$$

With a standard deviation that can be computed as [43,44]:

$$\Delta y = \sqrt{\sum_{i=1}^{n}\left(\left.\frac{\partial f}{\partial x_i}\right|_{\bar{x}_i}\right)^2 \left(\Delta x_i\right)^2} \tag{13}$$

Where $\left.\frac{\partial f}{\partial x_i}\right|_{\bar{x}_i}$ is the partial derivative of function *f* with respect to variable x_i, evaluated in the average value $\bar{x}_i$.

According to this method, the following standard deviations can be obtained for the observable $\delta^*\left(90^o, R\right)$, defined in equation (7):

$$\Delta\delta^*\left(90^o, R\right) = \sqrt{\left(\frac{1}{\overline{S_{TOT}\left(R\right)}}\right)^2 \left(\Delta S_{Dep}\left(90^o, R\right)\right)^2 + \left(\frac{\overline{S_{Dep}\left(90^o, R\right)}}{\overline{S_{TOT}\left(R\right)}^2}\right)^2 \left(\Delta S_{TOT}\left(R\right)\right)^2} \tag{14}$$

Where $\overline{S_{TOT}\left(R\right)}$ is the average value of the signal detected by the total power channel, as a function of range, $\overline{S_{Dep}\left(90^o, R\right)}$ is the average value of the signal detected by the depolarization channel (with the polarizer oriented 90o from the transmitted beam polarization, $\Delta S_{TOT}\left(R\right)$ is the standard deviation of the signal detected by the total power channel. $\Delta S_{Dep}\left(90^o, R\right)$ is the standard deviation of the signal detected by the depolarization channel.

According to the calibration method, the uncertainty associated to the estimation of the depolarization channel system function is reduced by the signal smoothing that is performed. According to the different calibrations presented in Fig. 8, an absolute error around $\left|\Delta V^*\left(R\right)\right| = 1$ will be considered in the computation of the error of the volume depolarization ratio, defined in equation (6):

$$\Delta\delta^V\left(R\right) = \sqrt{\left(\frac{V^*\left(R\right)}{V^*\left(R\right) - \delta^*\left(90^o, R\right)}\right)^2 \left(\Delta\delta^*\left(90^o, R\right)\right)^2 + \left(\frac{\delta^*\left(90^o, R\right)}{V^*\left(R\right) - \delta^*\left(90^o, R\right)}\right)^2 \left(V^*\left(R\right)\right)^2} \tag{15}$$

The computation of the error of the backscatter ratio, defined in equation (9), considers only the random variations of the retrieved particle backscatter ([30–33]):

$$\Delta\rho\left(R\right) = \sqrt{\left(\frac{1}{\beta^m\left(R\right)}\right)^2 \cdot \left(\Delta\beta^p\left(R\right)\right)^2} \tag{16}$$

Finally, for the computation of the error of the particle depolarization ratio, defined in equation (8), we will simplify the expression by defining:

$$Num(R) = \left[1+\delta^{m}\right]\cdot\delta^{V}(R)\cdot\rho(R) - \left[1+\delta^{V}(R)\right]\cdot\delta^{m}$$
$$Den(R) = \left[1+\delta^{m}\right]\cdot\rho(R) - \left[1+\delta^{V}(R)\right] \quad (17)$$

And then writing:

$$\Delta\delta\left({}^{p}(R)\right)^{2} = \left(\frac{\left[\left(1+\delta^{m}\right)\cdot\rho(R) - \delta^{m}\right]\cdot Den(R) + Num(R)}{\left(Den(R)\right)^{2}}\right)^{2}\cdot\left(\Delta\delta^{v}(R)\right)^{2} + \left(\frac{\left(1+\delta^{m}\right)\cdot\delta^{v}(R)\cdot Den(R) - \left(1+\delta^{m}\right)\cdot Num(R)}{\left(Den(R)\right)^{2}}\right)^{2}\cdot\left(\Delta\rho(R)\right) \quad (18)$$

References

1. D. Müller *et al.*, "Aerosol-type-dependent lidar ratios observed with Raman lidar," *J. Geophys. Res.*, vol. 112, no. D16, p. D16202, Aug. 2007. DOI: 10.1029/2006JD008292

2. B. A. Angstrom and T. Eppley, "The parameters of atmospheric turbidity," *Tellus*, vol. 16, no. 1, pp. 64–75, 1964. DOI: 10.1111/j.2153-3490.1964.tb00144.x

3. R. M. Schotland, K. Sassen, and R. Stone, "Observations by Lidar of Linear Depolarization Ratios for Hydrometeors," *Journal of Applied Meteorology*, vol. 10, no. 5. pp. 1011–1017, 1971. DOI: 10.1175/1520-0450(1971)010<1011:OBLOLD>2.0.CO;2

4. S. R. Pal and A. I. Carswell, "Polarization properties of lidar backscattering from clouds.," *Appl. Opt.*, vol. 12, no. 7, pp. 1530–1535, 1973. DOI: 10.1364/AO.12.001530

5. D. M. Winker and M. T. Osborn, "Airborne lidar observations of the Pinatubo volcanic plume," *Geophys. Res. Lett.*, vol. 19, no. 2, pp. 167–170, Jan. 1992. DOI: 10.1029/91GL02867

6. T. Murayama, D. Müller, K. Wada, A. Shimizu, M. Sekiguchi, and T. Tsukamoto, "Characterization of Asian dust and Siberian smoke with multi-wavelength Raman lidar over Tokyo, Japan in spring 2003," *Geophys. Res. Lett.*, vol. 31, no. 23, Dec. 2004. DOI: 10.1029/2004GL021105

7. A. M. Tafuro, F. Barnaba, F. De Tomasi, M. R. Perrone, and G. P. Gobbi, "Saharan dust particle properties over the central Mediterranean," *Atmos. Res.*, vol. 81, no. 1, pp. 67–93, Jul. 2006. DOI: 10.1016/j.atmosres.2005.11.008

8. M. Tesche *et al.*, "Vertical profiling of Saharan dust with Raman lidars and airborne HSRL in southern Morocco during SAMUM," *Tellus B*, vol. 61, no. 1, pp. 144–164, Feb. 2009. DOI: 10.1111/j.1600-0889.2008.00390.x

9. S. Groß *et al.*, "Characterization of the planetary boundary layer during SAMUM-2 by means of lidar measurements," *Tellus B Chem. Phys. Meteorol.*, vol. 63, no. 4, pp. 695–705, Jan. 2011. DOI: 10.1111/j.1600-0889.2011.00557.x

10. S. Groß *et al.*, "Characterization of Saharan dust, marine aerosols and mixtures of biomass-burning

aerosols and dust by means of multi-wavelength depolarization and Raman lidar measurements during SAMUM 2," *Tellus B Chem. Phys. Meteorol.*, vol. 63, no. 4, pp. 706–724, Jan. 2011. DOI: 10.1111/j.1600-0889.2011.00556.x

11. J. A. Bravo-Aranda *et al.*, "A new methodology for PBL height estimations based on lidar depolarization measurements: analysis and comparison against MWR and WRF model-based results," *Atmos. Chem. Phys*, vol. 17, pp. 6839–6851, 2017. DOI: 10.5194/acp-17-6839-2017

12. S. P. Burton *et al.*, "Aerosol classification using airborne High Spectral Resolution Lidar measurements-methodology and examples," *Atmos. Meas. Tech.*, vol. 5, no. 1, pp. 73–98, 2012. DOI: 10.5194/amt-5-73-2012

13. S. P. Burton *et al.*, "Observations of the spectral dependence of linear particle depolarization ratio of aerosols using NASA Langley airborne High Spectral Resolution Lidar," *Atmos. Chem. Phys.*, vol. 15, no. 23, pp. 13453–13473, 2015. DOI: 10.5194/acp-15-13453-2015

14. F. J. Olmo, A. Quirantes, V. Lara, H. Lyamani, and L. Alados-Arboledas, "Aerosol optical properties assessed by an inversion method using the solar principal plane for non-spherical particles," *J. Quant. Spectrosc. Radiat. Transf.*, vol. 109, no. 8, pp. 1504–1516, May 2008. DOI: 10.1016/j.jqsrt.2007.12.019

15. I. Veselovskii *et al.*, "Retrieval of optical and physical properties of African dust from multiwavelength Raman lidar measurements during the SHADOW campaign in Senegal," *Atmos. Chem. Phys*, vol. 16, pp. 7013–7028, 2016. DOI: 10.5194/acp-16-7013-2016

16. D. Müller, I. Veselovskii, A. Kolgotin, M. Tesche, A. Ansmann, and O. Dubovik, "Vertical profiles of pure dust and mixed smoke–dust plumes inferred from inversion of multiwavelength Raman/polarization lidar data and comparison to AERONET retrievals and in situ observations," *Appl. Opt.*, vol. 52, no. 14, p. 3178, May 2013. DOI: 10.1364/AO.52.003178

17. A. Chaikovsky *et al.*, "Lidar-Radiometer Inversion Code (LIRIC) for the retrieval of vertical aerosol properties from combined lidar/radiometer data: Development and distribution in EARLINET," *Atmos. Meas. Tech.*, vol. 9, no. 3, pp. 1181–1205, 2016. DOI: 10.5194/amt-9-1181-2016

18. G. Wandinger, Ulla; Ansmann, Albert; Mattis, Ina; Müller, Detlef; Pappalardo, "CALIPSO AND BEYOND: LONG-TERM GROUND-BASED SUPPORT OF SPACE-BORNE AEROSOLS AND CLOUD LIDAR MISSIONS," in *24th International Laser Radar Conference*, 2008, pp. 715–718. https://www.eol.ucar.edu/ilrc/ (retrieved on October 13th 2017)

19. A. Rodríguez-Gómez *et al.*, "DEPOLARIZATION CHANNEL FOR BARCELONA LIDAR. IMPLEMENTATION AND PRELIMINARY MEASUREMENTS," in *28th International Laser Radar Conference*, 2017, pp. 1–4. http://ilrc28.inoe.ro/ (retrieved on October 13th 2017)

20. D. Kumar *et al.*, "Six-channel polychromator design and implementation for the UPC elastic/Raman LIDAR," *SPIE Int. Symp. - Remote Sens. Eur.*, vol. 8182, p. 81820W–1–81820W–10, 2011. DOI: 10.1117/12.896305

411 21. V. Freudenthaler *et al.*, "Depolarization ratio profiling at several wavelengths in pure Saharan dust
412 during SAMUM 2006," *Tellus, Ser. B Chem. Phys. Meteorol.*, vol. 61, no. 1, pp. 165–179, 2009. DOI:
413 10.1111/j.1600-0889.2008.00396.x

414 22. D. Althausen *et al.*, "Scanning 6-Wavelength 11-Channel Aerosol Lidar," *J. Atmos. Ocean. Technol.*, vol.
415 17, no. 11, pp. 1469–1482, Nov. 2000. DOI: 10.1175/1520-0426(2000)017<1469:SWCAL>2.0.CO;2

416 23. U. Wandinger, "Introduction to Lidar," in *Lidar*, C. Weitkamp, Ed. New York: Springer-Verlag, 2005,
417 pp. 1–18. DOI: 10.1007/b106786

418 24. E. Vidal, "Disseny d'un canal de despolarització a 532 nm per al lidar d'EARLINET de la UPC,"
419 BarcelonaTech, 2013. http://hdl.handle.net/2099.1/18273 (retrieved on October 13th 2017)

420 25. Licel, "Transient Recorder Overview." [Online]. Available: http://licel.com/transient_overview.html.
421 [Accessed: 05-Jul-2017].

422 26. K. Sassen, "Polarization in Lidar," in *Lidar*, C. Weitkamp, Ed. New York: Springer-Verlag, 2005, pp. 19–
423 42. DOI: 10.1007/b106786

424 27. A. Comerón *et al.*, "Concept Design of a Multiwavelength Aerosol Lidar System With Mitigated
425 Diattenuation Effects and Depolarization-Measurement Capability," *EPJ Web Conf.*, vol. 119, no. 27th
426 International Laser Radar Conference, p. 23003, 2016. DOI: 10.1051/epjconf/201611923003

427 28. Licel, "Licel PM module." [Online]. Available: http://licel.com/DET-HV.htm. [Accessed: 05-Jul-2017].

428 29 J. D. Klett, "Stable analytical inversion solution for processing lidar returns," *Appl Opt*, vol. 20, no. 2, pp.
429 211–220, 1981. DOI: 10.1364/AO.20.000211

430 30. F. G. Fernald, "Analysis of atmospheric lidar observations: some comments," *Appl. Opt.*, vol. 23, no. 5,
431 pp. 652–653, Mar. 1984. DOI: 10.1364/AO.23.000652

432 31. A. Ansmann, M. Riebesell, and C. Weitkamp, "Measurement of atmospheric aerosol extinction profiles
433 with a Raman lidar," *Opt. Lett.*, vol. 15, no. 747, 1990. DOI: 10.1364/OL.15.000746

434 32. A. Ansmann, U. Wandinger, M. Riebesell, C. Weitkamp, and W. Michaelis, "Independent measurement
435 of extinction and backscatter profiles in cirrus clouds by using a combined Raman elastic-backscatter
436 lidar.," *Appl. Opt.*, vol. 31, no. 33, pp. 7113–7131, Nov. 1992. DOI: 10.1364/AO.31.007113

437 33. A. Behrendt and T. Nakamura, "Calculation of the calibration constant of polarization lidar and its
438 dependency on atmospheric temperature," *Opt. Express*, vol. 10, no. 16, p. 805, Aug. 2002. DOI:
439 10.1364/OE.10.000805

440 34. L. Belegante *et al.*, "Experimental assessment of the lidar polarizing sensitivity," *Atmos. Meas. Tech.*
441 *Discuss.*, February 2016, pp. 1–44, 2016. DOI: 10.5194/amt-2015-337

442 35. V. Freudenthaler, "About the effects of polarising optics on lidar signals and the +/-90º calibration",
443 *Atmos. Meas. Tech.*, vol. 9, no. 9, pp. 4181–4255, 2016. DOI: 10.5194/amt-9-4181-2016

36. M. Md. Reba, "Data processing and inversion interfacing the UPC elastic-Raman LIDAR system," BarcelonaTech University (UPC) 2010.

37. M. Sicard, R. Izquierdo, M. Alarcón, J. Belmonte, A. Comerón, and J. M. Baldasano, "Near-surface and columnar measurements with a micro pulse lidar of atmospheric pollen in Barcelona, Spain," *Atmos. Chem. Phys.*, vol. 16, no. 11, pp. 6805–6821, 2016. DOI: 10.5194/acp-16-6805-2016

38. J. Belmonte, "Personal Communication." 2017.

39. M. J. Costa *et al.*, "Main features of an outstanding desert dust transport over Iberia," in *5th Iberian Meeting on Aerosol Science and Technology (RICTA)*, 2017. http://www.ricta2017.org/

40 S. Groß, M. Esselborn, B. Weinzierl, M. Wirth, A. Fix, and A. Petzold, "Aerosol classification by airborne high spectral resolution lidar observations," *Atmos. Chem. Phys.*, vol. 13, no. 5, pp. 2487–2505, Mar. 2013. DOI: 10.5194/acp-13-2487-2013

41. K. Sassen and C. Hsueh, "Contrail properties derived from high-resolution lidar studies during SUCCESS after Lidar alepolarization ratios in persisting The PDL has been described previously so contrails clouds only the general and recent composed of high numbers of small particle," *Geophys. Res. Lett.*, vol. 25, no. 8, pp. 1165–1168, 1998. DOI: 10.1029/97GL03503

42. L. A. Goodman, "On the Exact Variance of Products," *J. Am. Stat. Assoc.*, vol. 55, no. 292, pp. 708–713, Dec. 1960. DOI: 10.1080/01621459.1960.10483369

43. H. H. Ku, "Notes on the use of propagation of error formulas," *J. Res. Natl. Bur. Stand. Sect. C Eng. Instrum.*, vol. 70C, no. 4, p. 263, 1966. DOI: 10.6028/jres.070C.025